ISSN 1674-1056
http://cpb.iphy.ac.cn
http://iopscience.iop.org/cpb
中国物理 B
Chinese Physics
中国物理
Chinese Physics B

Trajectory analysis of few-cycle strong field ionization in two-color circularly polarized fields

Yan Huang(黄燕), Chaochao Qin(秦朝朝), Yizhu Zhang(张逸竹), Xincheng Wang(王新成), Tian-Min Yan(阎天民), Yuhai Jiang(江玉海)

Citation: Chin. Phys. B . 2019, 28(9): 093202 . **doi:** 10.1088/1674-1056/28/9/093202
Journal homepage: http://cpb.iphy.ac.cn; http://iopscience.iop.org/cpb

What follows is a list of articles you may be interested in

Controlling Rydberg excitation process with shaped intense ultrashort laser pulses

Xiao-Yun Zhao(赵晓云), Chun-Cheng Wang(王春成), Shi-Lin Hu(胡师林), Wei-Dong Li(李卫东), Jing Chen(陈京), Xiao-Lei Hao(郝小雷)

Chin. Phys. B . 2019, 28(8): 083202 . **doi:** 10.1088/1674-1056/28/8/083202

Dependence of photoelectron-momentum distribution of H_2^+ molecule on orientation angle and laser ellipticity

Hong-Dan Zhang(张宏丹), Si-Qi Zhang(张思琪), Lei Ji(纪磊), Qi Zhen(甄琪), Jing Guo(郭静), Xue-Shen Liu(刘学深)

Chin. Phys. B . 2019, 28(5): 053201 . **doi:** 10.1088/1674-1056/28/5/053201

Femtosecond strong-field coherent control of nonresonant ionization with shaped pulses

Qiu-Nan Tong(佟秋男), Zhen-Zhong Lian(廉振中), Liang Zhao(赵亮), Hong-Xia Qi(齐洪霞), Zhou Chen(陈洲), Zhan Hu(胡湛)

Chin. Phys. B . 2019, 28(3): 033201 . **doi:** 10.1088/1674-1056/28/3/033201

Angle-resolved spectra of the direct above-threshold ionization of diatomic molecule in IR+XUV laser fields

Shang Shi(石尚), Fa-Cheng Jin(金发成), Bing-Bing Wang(王兵兵)

Chin. Phys. B . 2019, 28(2): 023202 . **doi:** 10.1088/1674-1056/28/2/023202

Validity of extracting photoionization time delay from the first moment of streaking spectrogram

Chang-Li Wei(魏长立), Xi Zhao(赵曦)

Chin. Phys. B . 2019, 28(1): 013201 . **doi:** 10.1088/1674-1056/28/1/013201

SPECIAL TOPIC — Strong-field atomic and molecular physics

Trajectory analysis of few-cycle strong field ionization in two-color circularly polarized fields*

Yan Huang(黄燕)[1], Chaochao Qin(秦朝朝)[1], Yizhu Zhang(张逸竹)[5], Xincheng Wang(王新成)[4], Tian-Min Yan(阎天民)[2,†], and Yuhai Jiang(江玉海)[2,3,4,1,‡]

[1] *College of Physics and Materials Science, Henan Normal University, Xinxiang* 453007, *China*
[2] *Shanghai Advanced Research Institute, Chinese Academy of Sciences, Shanghai* 201210, *China*
[3] *University of Chinese Academy of Sciences, Beijing* 100049, *China*
[4] *ShanghaiTech University, Shanghai* 201210, *China*
[5] *Key Laboratory of Opto-electronics Information and Technical Science, Tianjin University, Tianjin* 300072, *China*

(Received 21 May 2019; revised manuscript received 27 June 2019; published online 23 August 2019)

Bichromatic circularly polarized fields provide a useful tool to probe the ionization dynamics. In this work, we compare the photoelectron momentum distribution in few-cycle bichromatic field of different helicities. The spectral features are analyzed with semiclassical trajectories derived from the strong field approximation. In particular, the interference fringes in momentum distribution are investigated by tracking the ionization time and tunneling exits of released photoelectrons. Different types of trajectories that contribute to the interference fringes are elucidated.

Keywords: strong field ionization, semiclassical trajectories, bicircularly polarized fields, photoelectron momentum

PACS: 32.80.Rm, 42.50.Hz, 33.80.Wz **DOI:** 10.1088/1674-1056/ab3444

1. Introduction

Over the last decades, the advent of the free electron laser and strong table-based lasers has propelled both time-resolved spectroscopic and structural investigations of matter in many aspects.[1,2] As one among various strong field phenomena, the ionization process in bichromatic circularly polarized laser fields has recently sparked much interest. The interplay between two pulses results in complicated photoelectron dynamics, and yields intriguing strong field phenomena, e.g., helical vortex structures[3] and symmetrical patterns[4] in photoelectron momentum distributions. Especially, concerning the relative helicity of the two pulses (co-rotating and counter-rotating fields), the distinct distributions of lobes in photoelectron momentum distribution confirm the possibility to control the ionization dynamics by helicities.[4] Switching between the counter-rotating and co-rotating fields, the ionization path via excited states can be altered to dramatically change the ionization rate.[5] The photoelectron can be steered by the relative helicity to rescatter with its parent ion,[6] or to circumvent the recollision and smoothly escape the core. It has been shown that the double ionization may occur in counter-rotating fields which are delicately tuned to drive the photoelectron back to its parent ion,[7,8] opening possibilities for probing electronic and molecular structure by adjusting impact angles of complex trajectories of the rescattering electron.[9] Meanwhile, the counter-rotating fields introduce the momentum-dependent spin asymmetry of photoelectrons, suggesting the potential applications of spin-polarized electron in attoscience.[10] Also, the bicircular fields provide the access to new mechanism of radiation in strong fields. The recollision induced by counter-rotating fields has inspired the new approach to high-order harmonic generation (HHG),[11] allowing for the generation of circularly polarized soft x-ray pulses.[12,13] On the other hand, it is reported that the efficiency of terahertz (THz) emission in co-rotating circularly polarized laser fields is five times higher than that with linearly polarized two-color femtosecond pulses.[14] The significant enhancement of THz radiation utilizing the simple experimental setup undoubtedly broadens the application scenarios of intense THz light source.

Comparing to a linearly polarized field, the circularly polarized field extends the dimension of the driving force, by which the photoelectron can be maneuvered with the extra degree of freedom. The richer information may help unravel the structure and dynamics that could not be resolved before. For instance, the electronic structure and rotational symmetry in molecules can be traced out by photoelectron driven by the bichromatic fields.[15–17] In addition, using a circularly polarized femtosecond laser pulse, the technique of attosecond angular streaking, i.e., attoclock,[18,19] can transform the rota-

*Project supported by the National Natural Science Foundation of China (Grant Nos. 11420101003, 11604347, 11827806, 11874368, 61675213, and 91636105).
†Corresponding author. E-mail: yantm@sari.ac.cn
‡Corresponding author. E-mail: jiangyh@sari.ac.cn
© 2019 Chinese Physical Society and IOP Publishing Ltd

tion of the field polarization, which plays the role of the clock pointer, to the attosecond time resolution. Similarly, when bichromatic fields are present, a double-pointer attoclock can be designed by co-rotating field.[20] The photoelectron interferometer constituted by the two pointers allows probing the phase and the amplitude of photoelectron wave packets. Comparing the photoelectron distributions under counter- and co-rotating fields, the nonadiabatic offset of initial momentum distribution can also be easily assessed.[21] The attoclock using counter-rotating fields, on the other hand, allows for the clean investigation into the ionization steps in quasilinear polarization by inquiring the shift in the momentum distribution in the direction perpendicular to the momentum where the distribution peaks.[22] More subtle interference effects have also been studied. From the three-dimensional momentum distribution, the intra-cycle interference are observed by extracting from the momentum distribution along the light propagation direction.[23] The intensity-dependent interference structures have been observed, analogous to the spatially rotating temporal double-slit experiment with the variable slit width.[24] The interference can be dramatically affected by the Coulomb attraction of the parent ion or molecule since different paths of the electron wave packets are affected differently by the ionic potential.

In theory, the strong field approximation (SFA)[25–27] was widely used to investigate nonperturbative strong field physics. Based on the SFA, the interpretation in terms of electron trajectory derived from semiclassical approximation provides an intuitive understandings of various strong field processes, e.g., the well-known three-step model which explains the mechanism of the HHG. Especially since distinct types of trajectories are associated to different ionization pathways, semiclassical trajectories has been used to characterize the time delays of these pathways.[28,29] In addition, the concept of semiclassical trajectories provides a baseplate to incorporate effects that were not necessarily within the framework of the SFA, such as the long-range Coulomb interactions using trajectory-based Coulomb-corrected SFA[30–32] and analytical R-matrix theory.[33,34] The trajectories can also be easily evaluated in parallel, providing an efficient numerical method to investigate strong field dynamics. In this work, the method of the semiclassical trajectory has been extended to study the ionization dynamics in bichromatic circularly polarized fields. The selection of saddle points in circularly polarized fields is shown to be different from that in a linearly polarized field. Extra conditions are required to filter the solutions of saddle point equation. Utilizing the saddle points from the modified selection scheme, the initial conditions of trajectory calculation can be determined, and the procedure of further numerical calculation is the same as in a linearly polarized field.[31] Similar to the study in Ref. [35], we evaluate the photoelectron momentum distribution in a bichromatic circularly polarized fields, including a pulse of fundamental frequency (800 nm) and one of fifth-order frequency (160 nm). We focus on the formation of lobes and interference fringes under the few-cycle bichromatic circularly polarized fields in this work, presenting the comparison of spectral features between co-rotating and counter-rotating fields with trajectory analysis.

2. Theory and method

When an atom is subject to strong laser fields, nonperturbative ionization processes occur. The transition amplitude of the "direct" photoelectron with asymptotic momentum $\boldsymbol{p}$ is given by

$$M_{\boldsymbol{p}} = \int_{-\infty}^{\infty} \langle \boldsymbol{p} + \boldsymbol{A}(t') | \boldsymbol{E}(t') \cdot \boldsymbol{r} | \psi(t_0) \rangle \mathrm{e}^{-\mathrm{i} S_{\boldsymbol{p},I_\mathrm{p}}(t')} \mathrm{d}t', \quad (1)$$

with $|\psi(t_0)\rangle$ being the initial bound state of the electron, $\boldsymbol{A}(t)$ the vector potential of the light field, $\boldsymbol{E}(t) = -\partial_t \boldsymbol{A}(t)$ the electric field under the dipole approximation, and

$$S_{\boldsymbol{p},I_\mathrm{p}}(t) = \int^{t} \left[\frac{1}{2} (\boldsymbol{p} + \boldsymbol{A}(t'))^2 + I_\mathrm{p} \right] \mathrm{d}t'. \quad (2)$$

Here, I_p is the atomic ionization potential. The integral of Eq. (1) can be further simplified under the semiclassical approximation. Using the method of steepest descent,[36] the integral of Eq. (1) can be further reduced. Due to cancellation of sinusoids with rapidly varying phase of $S_{\boldsymbol{p},I_\mathrm{p}}(t)$, the integrand contributes only when $S_{\boldsymbol{p},I_\mathrm{p}}(t)$ approaches the stationary phase point, where the oscillation slows down. There may exist multiple such saddle points, as defined by $\{t_\mathrm{s}^{(\alpha)}\}$, that can be solved from the saddle point equation,

$$\frac{\partial S_{\boldsymbol{p},I_\mathrm{p}}(t)}{\partial t}\Big|_{t=t_\mathrm{s}^{(\alpha)}} = \frac{1}{2} \left[\boldsymbol{p} + \boldsymbol{A}\left(t_\mathrm{s}^{(\alpha)}\right) \right]^2 + I_\mathrm{p} = 0. \quad (3)$$

Hence, the method of steepest descent recasts integral (1) into the sum over all saddle points $\{t_\mathrm{s}\}$,

$$M_{\boldsymbol{p}} = -\frac{1}{\sqrt{2}} \left(2I_\mathrm{p}\right)^{\frac{5}{4}} \sum_i \frac{1}{S''_{\boldsymbol{p},I_\mathrm{p}}\left(t_\mathrm{s}^{(\alpha)}\right)} \mathrm{e}^{\mathrm{i} S_{\boldsymbol{p},I_\mathrm{p}}\left(t_\mathrm{s}^{(\alpha)}\right)}, \quad (4)$$

where $S''_{\boldsymbol{p},I_\mathrm{p}}$ denotes the second-order derivative of $S_{\boldsymbol{p},I_\mathrm{p}}$. The reduction into a sum not only avoids the heavy computation of the integration, but also derives the semiclassical approximation of the complicated nonperturbative strong field process. More intuitively, the ionization amplitude is the superposition of the contributions from semiclassical trajectories associated to all $\{t_\mathrm{s}^{(\alpha)}\}$. The fact can be clearly shown after taking some manipulation on Eq. (4) that leads to $M_{\boldsymbol{p}} = \sum_\alpha M_{\boldsymbol{p}}^{(\alpha)}$, where $M_{\boldsymbol{p}}^{(\alpha)} \propto \exp\left[-\mathrm{i} \int_{t_\mathrm{s}^{(\alpha)}}^{\infty} \left(\frac{1}{2}\boldsymbol{v}^2(t') + I_\mathrm{p}\right) \mathrm{d}t'\right] / S''(t_\mathrm{s}^{(\alpha)})$. Each α labels a trajectory and its velocity $\boldsymbol{v}(t) = \boldsymbol{p} + \boldsymbol{A}(t)$. For trajectory α starting from the initial time $t_\mathrm{s}^{(\alpha)}$, its kinematic quantities, e.g., $\boldsymbol{v}(t)$, are accumulated along this trajectory to contribute to a phase. In the end, the ionization amplitude is de-

termined by the superposition of these phases over all trajectories.

Note that $t_{\rm s}^{(\alpha)}$ is complex-valued, and the contour of integration should be specified to evaluate the integral. In this work, the contour for practical calculation consists of two straight paths in the complex time plane, $\int_{t_{\rm s}^{(\alpha)}}^{\infty} = \int_{t_{\rm s}^{(\alpha)}}^{t_{\rm r}^{(\alpha)}} + \int_{t_{\rm r}^{(\alpha)}}^{\infty}$, where $t_{\rm r}^{(\alpha)} = {\rm Re}\, t_{\rm s}^{(\alpha)}$. Along the two temporal paths, the imaginary time propagation for the sub-barrier region and real time propagation outside the barrier are conducted, respectively. For the imaginary time propagation, the propagation between $t_{\rm s}^{(\alpha)}$ and $t_{\rm r}^{(\alpha)}$ essentially describes the tunneling process. Here the simplest contour of integration is chosen—the parametric equation of the time contour is given by $t = t_{\rm r}^{(\alpha)} + {\rm i}\tau$, where τ varies from $\tau_0^{(\alpha)}$ to 0 with $\tau_0^{(\alpha)}$ satisfying $t_{\rm s}^{(\alpha)} = t_{\rm r}^{(\alpha)} + {\rm i}\tau_0^{(\alpha)}$. Here we have assumed that no real time is cost during the tunneling process. The initial time $t_{\rm s}^{(\alpha)}$ is when the electron starts entering the barrier, and the initial velocity is $\boldsymbol{v}(t_{\rm s}^{(\alpha)}) = \boldsymbol{p} + \boldsymbol{A}(t_{\rm s}^{(\alpha)})$. Since the displacement is of the form $\boldsymbol{r}(t) = \int^t \boldsymbol{v}(t'){\rm d}t'$, if we assume that the electron is initially located at the origin in the real space, i.e., ${\rm Re}\,\boldsymbol{r}(t_{\rm s}^{(\alpha)}) = 0$, straightforwardly we have the sub-barrier trajectory $\boldsymbol{r}(t) = \int_0^t \boldsymbol{v}(t'){\rm d}t' - {\rm Re}\int_0^{t_{\rm s}^{(\alpha)}} \boldsymbol{v}(t'){\rm d}t'$. On the other hand, at $t_{\rm r}^{(\alpha)}$ when the imaginary time propagation ends, the electron reaches the "tunneling exit" $\boldsymbol{r}(t_{\rm r}^{(\alpha)})$ where the electron emerges in the real space. During the subsequent real time propagation, all kinematic quantities become real-valued, and the trajectory now is given by $\boldsymbol{r}(t) = \int_{t_{\rm r}^{(\alpha)}}^t \boldsymbol{v}(t'){\rm d}t' + \boldsymbol{r}(t_{\rm r}^{(\alpha)})$.

The numerical implementation of the trajectory-based calculation starts with the sampling of the asymptotic momentum $\boldsymbol{p}$ within an appropriate parametric range. In the absence of the Coulomb potential, we have $\boldsymbol{v}(t) \to \boldsymbol{p}$ with $\boldsymbol{A}(\infty) \to 0$. Therefore, the range of samping $\boldsymbol{p}$ directly maps to the range of the measured photoelectron momentum. Given a specified $\boldsymbol{p}$, a series of $t_{\rm s}^{(\alpha)}$ can be solved from the saddle point equation (3) using complex root searching routines. Given the initial time $t_{\rm s}^{(\alpha)}$, all kinematic quantities can be evaluated and $M_{\boldsymbol{p}}$ can be eventually obtained. Therefore, the key to the numerical calculation is to find all $t_{\rm s}^{(\alpha)}$.

We emphasize that not all roots of Eq. (3) are saddle points $t_{\rm s}^{(\alpha)}$ and extra conditions may be required to select the appropriate ones. For instance, the $t_{\rm s}^{(\alpha)}$ distribution under a circularly polarized field is distinct from the linearly polarized field. In a linearly polarized field of $N_{\rm c}$ cycles, all $2(N_{\rm c}+1)$ roots are valid saddle points, effectively contributing to $M_{\boldsymbol{p}}$. In a field of more complicated form, however, some roots are not saddle points. The errorous inclusion of these roots may result in the divergent $M_{\boldsymbol{p}}$. Taking the bicircular fields for instance, the distribution of all roots of Eq. (3) are shown in Fig. 1. We note that the two points marked by green circles lead to divergent ionization yields. These artificial points are featured by either ${\rm Im}\, S''_{\boldsymbol{p},I_{\rm p}}(t_{\rm s}^{(\alpha)}) < 0$ or $\left|{\rm Re}\, S''_{\boldsymbol{p},I_{\rm p}}(t_{\rm s}^{(\alpha)})\right| \gg 0$. In the method of steepest descent, ${\rm Im}\left[{\rm i}S_{\boldsymbol{p},I_{\rm p}}(t)\right]$ is along a constant contour and ${\rm Re}\left[{\rm i}S_{\boldsymbol{p},I_{\rm p}}(t)\right]$ moves along the path of the steepest descent around the saddle point $t_{\rm s}^{(\alpha)}$. Assuming an infinitesimal step h along the contour,

$$
\begin{aligned}
{\rm Re}\left[{\rm i}S(t_{\rm s}^{(\alpha)}+h)\right] &< {\rm Re}\left[{\rm i}S(t_{\rm s}^{(\alpha)})\right], &(5)\\
{\rm Im}\left[{\rm i}S(t_{\rm s}^{(\alpha)}+h)\right] &= {\rm Im}\left[{\rm i}S(t_{\rm s}^{(\alpha)})\right]. &(6)
\end{aligned}
$$

Expanding $S(t_{\rm s}^{(\alpha)}+h) = S(t_{\rm s}^{(\alpha)}) + S'(t_{\rm s}^{(\alpha)})h + \frac{1}{2}S''(t_{\rm s}^{(\alpha)})h^2 + \cdots$ and using Eq. (3), $S'(t_{\rm s}^{(\alpha)}) = 0$, it is shown from Eq. (5) that ${\rm Re}[{\rm i}S''(t_{\rm s}^{(\alpha)})] < 0$, i.e.,

$$
{\rm Im}\left[S''(t_{\rm s}^{(\alpha)})\right] > 0. \tag{7}
$$

Similarly, according to Eq. (6), it is shown that

$$
{\rm Re}\left[S''(t_{\rm s}^{(\alpha)})\right] \simeq 0. \tag{8}
$$

Equations (7) and (8) exactly explain the failure mentioned above, and these two conditions should be imposed to select $t_{\rm s}^{(\alpha)}$.

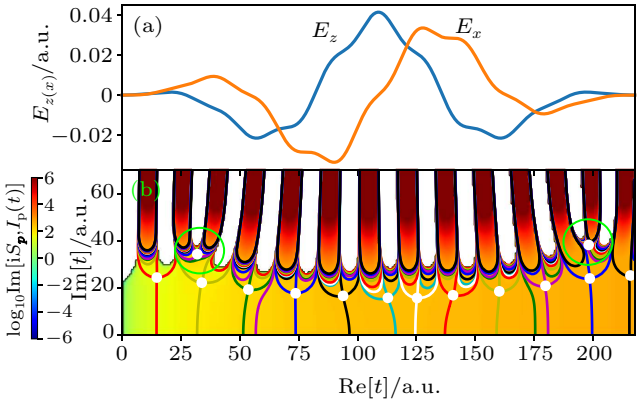


Fig. 1. Distribution of saddle points in circularly polarized fields. Panel (a) shows z (blue) and x (orange) components in a bicircularly polarized fields. Taking an initial momentum $\boldsymbol{p}_0 = (0.8, -0.8)$ for instance, the distribution of roots of Eq. (3) in the complex time plane is presented in panel (b). The contour lines represent the ${\rm Im}[{\rm i}S(t)]$ that pass via all $t_{\rm s}^{(\alpha)}$. Each $t_{\rm s}^{(\alpha)}$ is indicated by a white marker. Invalid solutions that do not obey conditions (7) and (8) are indicated by green circles.

3. Results and discussion

Under the bicircular laser fields, the momentum distributions for both co-rotating and counter-rotating field are investigated with trajectory analysis. The components of bicircular laser fields are given by

$$
\begin{aligned}
E_z(t) &= \frac{1}{\sqrt{2}}\sin^2\left(\frac{\omega t}{2N_{\rm c}}\right)\left[E_1\cos(\omega t) + E_q\cos(q\omega t)\right],\\
E_x(t) &= \frac{1}{\sqrt{2}}\sin^2\left(\frac{\omega t}{2N_{\rm c}}\right)\left[E_1\sin(\omega t) \pm E_q\sin(q\omega t)\right], \qquad (9)
\end{aligned}
$$

consisting of a fundamental harmonic field of frequency ω and a qth-order harmonic field of frequency $q\omega$. The sign of "+" ("−") forms the co-rotating (counter-rotating) fields. The field

amplitudes of the two-color fields are E_1 and E_q, respectively. In this work, the study focuses on the few-cycle case when the qth order harmonic field can be considered perturbation to the fundamental harmonic field. Here, $N_c = 2$, $q = 5$, and $E_1 : E_q = 10 : 1$ are chosen. In Fig. 2, the momentum distributions for co- and counter-rotating fields are shown in panels (a) and (b), respectively, showing the different numbers of lobes. The number is $q-1=4$ for the co-rotating fields and $q+1=5$ for the counter-rotating fields, in agreement with the spatial patterns of vector potential $\boldsymbol{A}(t)$ as indicated by the red lines. Besides, interference fringes emerge on the upper plane for both (a) and (b). The origin of interference patterns can be traced back via trajectories. Hence, points "a", "b", "c", and "d" are selected to analyze the formation of the interference on the momentum spectrum under the few-cycle bicircular fields.

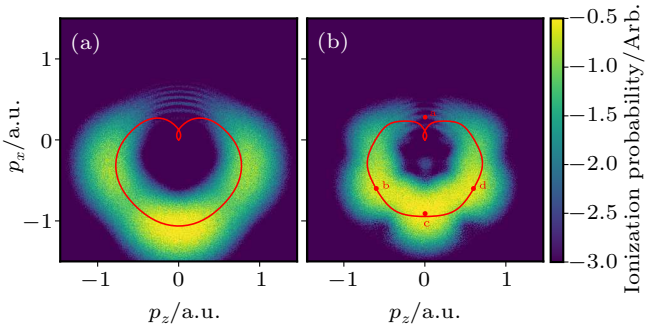


Fig. 2. Momentum distribution and the vector potential (red line) for (a) co-rotating and (b) counter-rotating fields. Points a, b, c, and d are marked for trajectory analysis as presented in the main text.

Taking sample point "a" for instance, all trajectories of the asymptotic momentum around "a" are selected. The temporal distribution of their tunneling time $t_r^{(\alpha)}$ and the spatial distribution of tunneling exits $\boldsymbol{r}(t_r^{(\alpha)})$ are shown by scatter points of different colors in Figs. 3(a) and 3(b), respectively. Defining the size of the scatter point proportional to $|M_{\boldsymbol{p}}^{(\alpha)}|$, i.e., the weight of trajectory α, a larger point represents the ionization event of higher probability. The components of laser fields are also presented for reference. The bicircular fields shows a symmetrically hexagonal distribution of polarization. Scatter points 1 and 2 indicate the most probable tunneling times $t_r^{(\alpha)}$ and tunneling exits $\boldsymbol{r}(t_r^{(\alpha)})$. They originate from different cycles of laser pulse, as shown in panel (a), while almost emerge from the same tunneling exit near $\boldsymbol{r}(t_r^{(\alpha)}) = (6, 0)$, as shown in panel (b).

Starting with $t_r^{(\alpha)}$ and the associated initial variables as presented in Fig. 3, all trajectories propagating in real space are shown in Fig. 4, with their weights defined by $|M_p^{(\alpha)}|$. According to the spatial profile, two types of trajectories, the long one T1, including trajectories 1, 3, 5, 7, and 9, can be distinguished from the short one T2, trajectories 2, 4, 6, 8, and 10. As shown in Fig. 3(a), trajectories of T1 tunnel through the potential barrier during the first half of the pulse, and subsequently spend longer time propagating in real space. In contrast, $t_r^{(\alpha)}$ of T2 are within the last half and the trajectories are short. Besides the difference in $t_r^{(\alpha)}$, in Fig. 4, the initial velocity $v_z(t_r^{(\alpha)})$ of trajectories T1 in the z-direction is positive, while $v_z(t_r^{(\alpha)})$ of trajectories T2 are negative.

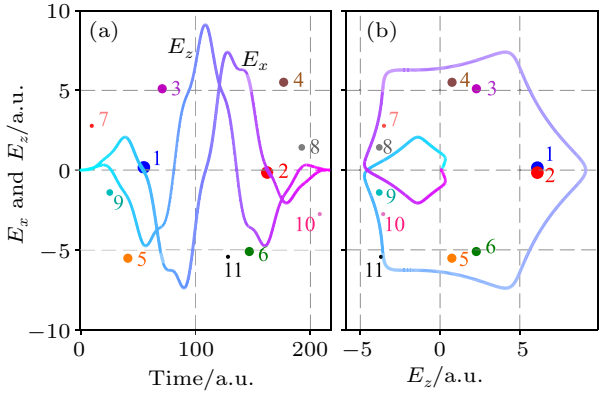


Fig. 3. The distributions of tunneling time and tunneling exit of photoelectron trajectories. In panel (a), the ionization time t_r are shown by scatter points. The electric components of light fields, $E_z(t)$ and $E_x(t)$, are shown by solid lines, whose gradient colors indicate the time evolution. In panel (b), distribution of tunneling exits and the spatial profile of laser fields are presented. The gradient colors in panels (a) and (b) are mapped to the same time.

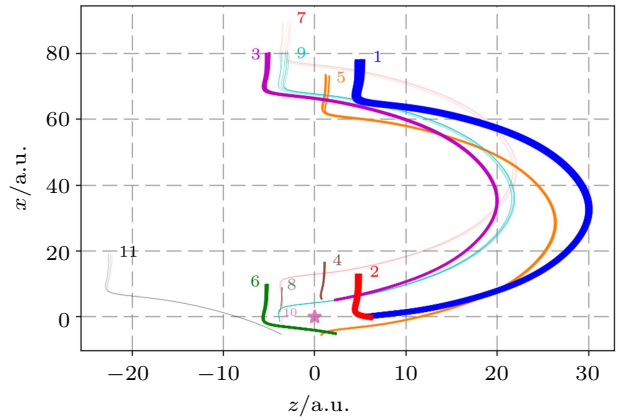


Fig. 4. Photoelectron trajectories in counter-rotating fields starting with the initial time $t_r^{(\alpha)}$ as shown in Fig. 3(b) of the same color code.

From the spatial distribution of $\boldsymbol{r}(t_r^{(\alpha)})$, the tunneling exits are roughly positioned at vertices of a hexagon, similar to the external light fields. Noteworthily, according to Fig. 3(b), though trajectories 1 and 2 have the largest weights, their ionization time are not when the absolute value of light fields reaches the maximum, which is different from the ionization process in a linearly polarized field.

The above analysis focuses on point "a" in Fig. 2(b) which shows interference fringes in momentum spectrum. By comparison, another three sample points "b", "c", and "d" without interference fringes have also been studied. As shown by spatial and temporal distributions of trajectories, in any region marked by "b", "c", or "d", one group of trajectories has much larger ionization probability amplitudes than others, which renders the significant interference impossible. The

presence of at least a pair of trajectories of comparable ionization probabilities is the prerequisite to form significant interference patterns.

In Figs. 2(a) and 2(b), the details of interference fringes within one cycle are present for both the co-rotating and counter-rotating fields. Phase analysis of trajectories allows interpreting the formation of the interference fringes. We select a series of sample points along the p_x-direction for both co-rotating and counter-rotating fields, as shown by Figs. 5(a) and 5(c). For each point of a given asymptotic momentum, the trajectories are collected to evaluate the average of the associated $M_{\boldsymbol{p}}^{(\alpha)}$. The distributions of the averaged $M_{\boldsymbol{p}}^{(\alpha)}$ in the complex plane are shown in Figs. 5(b) and 5(d), respectively, for the counter-rotating and co-rotating fields. Blue and red points are shown in the scatter plot, representing the $M_{\boldsymbol{p}}^{(\alpha)}$ of the dominant two groups of trajectories 1 and 2, respectively. From samples 1–14 as shown in panels (a) and (c), the $M_{\boldsymbol{p}}^{(\alpha)}$ of both types rotate counterclockwisely at different angular speeds as shown in panels (b) and (d). When $M_{\boldsymbol{p}}^{(\alpha)}$ of the two interfering trajectories are of the same phase, i.e., pointing to the same directions, the constructive interference leads to the peak of the interference fringes, e.g., point 5 in Figs. 5(a) and 5(b). Otherwise, the opposite directions from $M_{\boldsymbol{p}}^{(\alpha)}$ form a valley in the momentum distribution, e.g., point 14 in panels (a) and (b). Notably, the changes of interference fringes induced by counter-rotating and co-rotating fields are different. Comparing with the momentum distribution under the co-rotating fields in Fig. 5(c), the fringes for counter-rotating fields, as shown by Fig. 5(a), are denser. The fast modulation of the fringes resides in the high relative "rotation" speed of the $M_{\boldsymbol{p}}^{(\alpha)}$ (Fig. 5(b)).

The formation of interference patterns is also studied by increasing N_c of the few-cycle laser fields. In Fig. 6(a), when $N_c = 3$, interference-induced honeycomb structures are shown all over the spectrum, in contrast to the presence of interference fringes only along the p_x-axis when $N_c = 2$. Two sample points along p_z-axis, as shown in Fig. 6(a), are selected to analyze the interference structure induced by the extra optical cycle. In Figs. 6(b) and 6(e), the distributions of tunneling exits for the two samples points are shown respectively. It is found that the two types of dominant trajectories yield the interference. Photoelectrons of negative (positive) p_z originate from the tunneling exits on the upper (lower) plane. In Figs. 6(c) and 6(f), the distributions of tunneling time are shown. The tunneling time of the dominant two types of trajectories are within the same optical cycle, similar to "short" and "long" trajectories in a linearly polarized field. Therefore, the presence of interference structure is due to the intra-cycle interference. In Figs. 6(d) and 6(g), the associated trajectories in real space are presented. Comparing with interference effects for $N_c = 2$ where the $\boldsymbol{r}(t_r^{(\alpha)})$ of the interfering trajectories are almost the same while their $t_r^{(\alpha)}$ are different. When $N_c = 3$, the $t_r^{(\alpha)}$ shown in Figs. 6(c) and 6(f) are located around the peak of the laser pulse, while $\boldsymbol{r}(t_r^{(\alpha)})$ are distributed in the forward and backward directions with respect to $p_z = 0$.

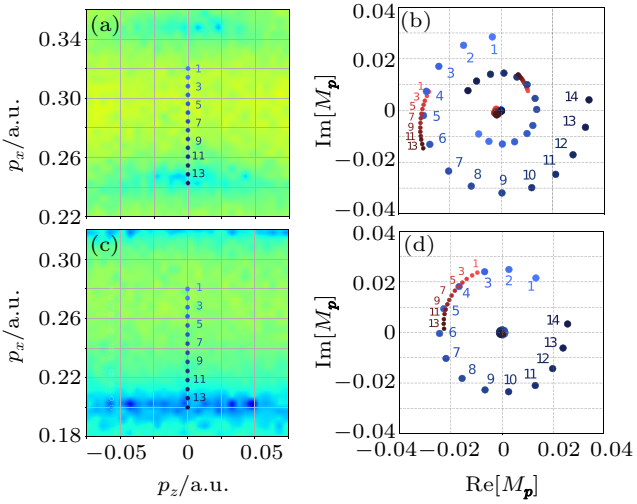


Fig. 5. The sample points in momentum distribution and the corresponding $M_{\boldsymbol{p}}^{(\alpha)}$ in the complex plane. In panels (a) and (c), the selected sample points around the interference fringes are shown in the zoom view of momentum distribution as presented in Figs. 2(b) (counter-rotating) and 2(a) (co-rotating), respectively, for counter-rotating and co-rotating fields. The averaged complex-valued $M_{\boldsymbol{p}}^{(\alpha)}$ of trajectories, whose asymptotic momenta are within the bin indicated by points in panels (a) and (c), are presented in panels (b) and (d), respectively. The dominant types of trajectories are distinguished by different colors.

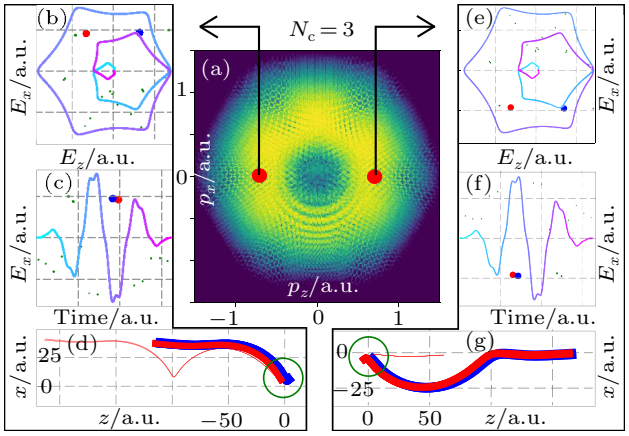


Fig. 6. Photoelectron momentum distribution in counter-rotating fields of $N_c = 3$ is shown in panel (a). Two sample points, as indicated by red marks, are chosen for trajectory analysis. The tunneling time, tunneling exits and the trajectories are shown in panels (b)–(d) [(e)–(g)] for the left (right) sample point, respectively. Green circle in panels (d) and (g) indicates the starting position of trajectories.

4. Conclusion

We have extended the semiclassical trajectory analysis to study the photoelectron momentum distribution in few-cycle bichromatic circularly polarized fields. When applying the method of the semiclassical trajectory, unlike the selection rule of saddle points for a linearly polarized field, in general, the solutions to the saddle point equation have to be filtered by imposing extra conditions. Evaluating the photoelectron momen-

tum distributions with semi-classical trajectories, the work focuses on the comparison of lobes and interference patterns under the few-cycle co-rotating and counter-rotating fields. In this work, the field of fundamental frequency is assumed to be stronger than the field of qth order harmonic frequency. The photoelectron momentum distributions present different patterns of lobes and modulated interference fringes. The spectral features can be explored via tracking trajectories that contribute to the asymptotic momentum of interest. Especially under the few-cycle laser fields, the formation of interference can be elucidated by pinpointing all interfering trajectories. When the ionization probabilities of interfering trajectories are comparable, interference fringes become significant. The fringes along p_z-axis for $N_c = 3$ originate from the interference between a pair of trajectories from within the same cycle, similar to the intra-cycle interference in a linearly polarized field. More intriguingly, the interference fringes along p_x-axis are already present when $N_c = 2$, which do not have the counterpart in a linearly polarized field. These fringes are shown to be caused by interference between trajectories of almost the same tunneling exits but from different cycles. Using bichromatic fields, it leaves open the possibility to investigate dynamics of photoelectron from given tunneling exits, e.g., the sub-barrier propagation accumulated phase during the tunneling process,[37,38] via the phase information encoded in the interference structure.

References

[1] Zhang Y Z and Jiang Y H 2015 *Advances of Atoms and Molecules in Strong Laser Fields: Imaging Ultra-fast Molecular Dynamics in Free Electron Laser Field* (WORLD SCIENTIFIC) pp. 205–235

[2] Zhang Y Z, Yan T M and Jiang Y H 2018 *Phys. Rev. Lett.* **121** 113201

[3] Ngoko Djiokap J M, Hu S X, Madsen L B, Manakov N L, Meremianin A V and Starace A F 2015 *Phys. Rev. Lett.* **115** 113004

[4] Mancuso C A, Hickstein D D, Grychtol P, Knut R, Kfir O, Tong X M, Dollar F, Zusin D, Gopalakrishnan M, Gentry C, Turgut E, Ellis J L, Chen M C, Fleischer A, Cohen O, Kapteyn H C and Murnane M M 2015 *Phys. Rev. A* **91** 031402

[5] Mancuso C A, Dorney K M, Hickstein D D, Chaloupka J L, Tong X M, Ellis J L, Kapteyn H C and Murnane M M 2017 *Phys. Rev. A* **96** 023402

[6] Mancuso C A, Hickstein D D, Dorney K M, Ellis J L, Hasović E, Knut R, Grychtol P, Gentry C, Gopalakrishnan M, Zusin D, Dollar F J, Tong X M, Milošević D B, Becker W, Kapteyn H C and Murnane M M 2016 *Phys. Rev. A* **93** 053406

[7] Mancuso C A, Dorney K M, Hickstein D D, Chaloupka J L, Ellis J L, Dollar F J, Knut R, Grychtol P, Zusin D, Gentry C, Gopalakrishnan M, Kapteyn H C and Murnane M M 2016 *Phys. Rev. Lett.* **117** 133201

[8] Eckart S, Richter M, Kunitski M, Hartung A, Rist J, Henrichs K, Schlott N, Kang H, Bauer T, Sann H, Schmidt L, Schöffler M, Jahnke T and Dörner R 2016 *Phys. Rev. Lett.* **117** 133202

[9] Chaloupka J L and Hickstein D D 2016 *Phys. Rev. Lett.* **116** 143005

[10] Milošević D B 2016 *Phys. Rev. A* **93** 051402

[11] Milošević D B, Becker W and Kopold R 2000 *Phys. Rev. A* **61** 063403

[12] Fleischer A, Kfir O, Diskin T, Sidorenko P and Cohen O 2014 *Nat. Photon.* **8** 543

[13] Kfir O, Grychtol P, Turgut E, Knut R, Zusin D, Popmintchev D, Popmintchev T, Nembach H, Shaw J M, Fleischer A, Kapteyn H, Murnane M and Cohen O 2015 *Nat. Photon.* **9** 99

[14] Meng C, Chen W, Wang X, Lü Z, Huang Y, Liu J, Zhang D, Zhao Z and Yuan J 2016 *Appl. Phys. Lett.* **109** 131105

[15] Lin K, Jia X, Yu Z, He F, Ma J, Li H, Gong X, Song Q, Ji Q, Zhang W, Li H, Lu P, Zeng H, Chen J and Wu J 2017 *Phys. Rev. Lett.* **119** 203202

[16] Habibović D, Čerkić A, Busuladžić M, Gazibegović-Busuladžić A, Odžak S, Hasović E and Milošević D B 2018 *Opt. Quant. Electron.* **50** 214

[17] Gazibegović-Busuladžić A, Busuladžić M, Hasović E, Becker W and Milošević D B 2018 *Phys. Rev. A* **97** 043432

[18] Eckle P, Pfeiffer A N, Cirelli C, Staudte A, Dörner R, Muller H G, Büttiker M and Keller U 2008 *Science* **322** 1525

[19] Eckle P, Smolarski M, Schlup P, Biegert J, Staudte A, Schöffler M, Muller H G, Dörner R and Keller U 2008 *Nat. Phys.* **4** 565

[20] Han M, Ge P, Shao Y, Gong Q and Liu Y 2018 *Phys. Rev. Lett.* **120** 073202

[21] Eckart S, Fehre K, Eicke N, Hartung A, Rist J, Trabert D, Strenger N, Pier A, Schmidt L, Jahnke T, Schöffler M, Lein M, Kunitski M and Dörner R 2018 *Phys. Rev. Lett.* **121** 163202

[22] Eicke N and Lein M 2019 *Phys. Rev. A* **99** 031402

[23] Eckart S, Kunitski M, Ivanov I, Richter M, Fehre K, Hartung A, Rist J, Henrichs K, Trabert D, Schlott N, Schmidt L P H, Jahnke T, Schöffler M S, Kheifets A and Dörner R 2018 *Phys. Rev. A* **97** 041402

[24] Ge P, Han M, Deng Y, Gong Q and Liu Y 2019 *Phys. Rev. Lett.* **122** 013201

[25] Keldysh L V 1965 *Zh. Eksp. Teor. Fiz. (Sov. Phys. JETP)* **47** 1945

[26] Faisal F H M 1973 *J. Phys. B: Atom. Mol. Phys.* **6** L89

[27] Reiss H R 1980 *Phys. Rev. A* **22** 1786

[28] Gong X, Lin C, He F, Song Q, Lin K, Ji Q, Zhang W, Ma J, Lu P, Liu Y, Zeng H, Yang W and Wu J 2017 *Phys. Rev. Lett.* **118** 143203

[29] Song X, Shi G, Zhang G, Xu J, Lin C, Chen J and Yang W 2018 *Phys. Rev. Lett.* ***121*** *103201*

[30] Popruzhenko S and Bauer D 2008 *J. Mod. Opt.* **55** 2573

[31] Yan T M, V Popruzhenko S, J J Vrakking M and Bauer D 2010 *Phys. Rev. Lett.* **105** 253002

[32] Li M, Geng J W, Liu H, Deng Y, Wu C, Peng L Y, Gong Q and Liu Y 2014 *Phys. Rev. Lett.* **112** 113002

[33] Torlina L and Smirnova O 2012 *Phys. Rev. A* **86** 043408

[34] Huang W X, Zhang Y Z, Yan T M and Jiang Y H 2016 *Acta Phys. Sin.* **65** 223204 (in Chinese)

[35] Ivanov I A, Nam C H and Kim K T 2017 *Phys. Rev. A* **95** 053401

[36] Deift P and Zhou X 1993 *Ann. Math.* **137** 295

[37] Yan T M and Bauer D 2012 *Phys. Rev. A* **86** 053403

[38] Han M, Ge P, Shao Y, Liu M M, Deng Y, Wu C, Gong Q and Liu Y 2017 *Phys. Rev. Lett.* **119** 073201